

VPIT: Real-time Embedded Single Object 3D Tracking Using Voxel Pseudo Images

Illia Oleksiienko*, Paraskevi Nousi†, Nikolaos Passalis†, Anastasios Tefas† and Alexandros Iosifidis*

*Department of Electrical and Computer Engineering, Aarhus University, Denmark

†Department of Informatics, Aristotle University of Thessaloniki, Greece

{io, ai}@ece.au.dk {paranous, passalis, tefas}@csd.auth.gr

Abstract—In this paper, we propose a novel voxel-based 3D single object tracking (3D SOT) method called Voxel Pseudo Image Tracking (VPIT). VPIT is the first method that uses voxel pseudo images for 3D SOT. The input point cloud is structured by pillar-based voxelization, and the resulting pseudo image is used as an input to a 2D-like Siamese SOT method. The pseudo image is created in the Bird’s-eye View (BEV) coordinates, and therefore the objects in it have constant size. Thus, only the object rotation can change in the new coordinate system and not the object scale. For this reason, we replace multi-scale search with a multi-rotation search, where differently rotated search regions are compared against a single target representation to predict both position and rotation of the object. Experiments on KITTI Tracking dataset show that VPIT is the fastest 3D SOT method and maintains competitive Success and Precision values. Application of a SOT method in a real-world scenario meets with limitations such as lower computational capabilities of embedded devices and a latency-unforgiving environment, where the method is forced to skip certain data frames if the inference speed is not high enough. We implement a real-time evaluation protocol and show that other methods lose most of their performance on embedded devices, while VPIT maintains its ability to track the object.

Index Terms—3D tracking, single object tracking, voxels, pillars, pseudo images, real-time neural networks, embedded deep learning (DL)

I. INTRODUCTION

WITH the rise of robotics usage in real-world scenarios, there is a need to develop methods for understanding the 3D world in order to allow a robot to interact with objects. To this end, efficient methods for 3D object detection, tracking, and active perception are needed. Such methods provide the main source of information for scene understanding, as having high-quality object detection and tracking outputs increases chances for a successful interaction with surroundings.

While for 2D perception tasks mainly cameras are used, there is a variety of sensors that can be used for 3D perception tasks, ranging from inexpensive solutions like single or multiple cameras to more costly ones like Lidar or Radar. Lidar is currently a well-adopted choice for 3D perception methods as it creates a set of 3D points forming a point cloud taken by shooting laser beams in multiple directions and counting the time needed for a reflection to be sensed. Point cloud data, despite being sparse and irregular, contains

much more information needed for 3D perception compared to images, and is more robust to changes in weather and lightning conditions. 3D object detection and tracking methods using point clouds provide the best combination of accuracy and inference speed, as can be seen in the KITTI leaderboard [1].

Lidars usually operate at 10-20 FPS, and therefore, a method receiving point cloud data as input can be called real-time if its inference speed is at the rate of the Lidar’s data generation, as it will not be able to receive more data to process. Even when the method cannot benefit from the FPS, higher than the Lidar’s frame rate, perception methods are usually paired with another method that makes use of the perception results, as in planning tasks. This means that the saved processing time in between Lidar’s frames can be used to analyze the results of the tracking without affecting its performance. In case of insufficient total frame rate, that can happen due to a slower computing system and higher additional computational load, tracking methods can suffer from dropped frames, that cannot be processed because the system is busy processing a previous data frame. This will result in worse tracking results and, in case of high drop rate, it may make the method unusable.

3D SOT, in contrast to the multiple 3D object tracking (3D MOT) task, focuses on tracking a single object of interest with a given initial frame position. This task lies between object detection and multiple object tracking tasks, as the latter one requires objects to be detected first, and then to associate each of them to a previously observed object. SOT methods do not rely on object detection, but they try to find the object offset on a new frame either by using correlation filters [2], [3], or deep learning models that regress to the predicted object offset [4], or use a Siamese approach to find the position with the highest similarity [5]–[8], or use voting [9], [10].

Application of tracking methods for real-world tasks meets a problem where, due to the model’s latency, not all data frames can be processed [11], [12]. For single-frame tasks, such as object detection, this problem only influences the latency of the predictions and not their quality, but in tracking, the connection between consecutive frames is important. This means that dropping frames can result in wrong associations for MOT or in a lost object for SOT. Methods like those mentioned above do not take into consideration the limited computational capabilities of embedded computing devices, which are typically used in robotics applications, e.g., self-driving cars, due to a lower power consumption that allows the robotic system to stay active for a longer time. These devices

This work has received funding from the European Union’s Horizon 2020 research and innovation programme under grant agreement No 871449 (OpenDR).

have a different architecture of CPU-GPU communication than desktop computers and high-end workstations. Thus, depending on the CPU-GPU workload balance and communication protocol of a robotic system, some methods can be better suited for achieving real-time operation.

In this paper, we present a novel method for 3D SOT receiving voxel pseudo images as an input, as opposed to point-based models proposed for 3D SOT. Voxel pseudo images are created in Bird’s-eye View (BEV) coordinates, and since the objects in such projection do not change size, we remove the standard multiscale search process followed by 2D SOT methods. We propose the use of multi-rotation search, where differently rotated search regions are compared against a single target representation to predict both the position and rotation of the object. We show that adopting such an approach leads to fast tracking with competitive performance compared to the point-based methods. This opens a possibility to adapt 2D SOT methods for a 3D task with minor changes. Considering real-world limitations, we follow [11] and implement a benchmark for real-time Lidar-based 3D SOT on embedded devices, showcasing the performance drop of the fastest methods when implemented in a real-world scenario.

The remainder of the paper is organized as follows: Section II provides a description of the related works. Section III describes the proposed method, along with the proposed training and inference processes. Section IV provides evaluation results on high-end and embedded devices with consideration of real-time requirements. Section V concludes the paper and formulates directions for future work.

II. RELATED WORKS

SOT in 3D is commonly formulated as an extension of 2D SOT. In both cases, an initial position of the object of interest is given, and the method needs to predict the position of the object in all future frames. The main difference between 2D and 3D SOT rises from the type of data used as input. Camera-based 3D perception methods commonly achieve poor performance due to the increased difficulty of extracting correct spatial information from cameras, and therefore most of the 3D object tracking methods use point cloud data or a combination of point clouds and camera images. Point cloud sparsity does not allow using straightforward extensions of 2D SOT methods based on regular CNNs.

SC3D [13] uses a Siamese approach by encoding a target point cloud shape in the initial frame and searching for regions in a new frame with the smallest cosine distance between target and search encodings. After finding a new location, the new object shape is combined with the previous one to increase the quality of comparison in future frames. It achieves good tracking results, but its operation is computationally expensive. Assuming that an object should not move far away from its current location in consecutive frames, one can define a search region inside its neighborhood for searching it in a new frame. This is commonly done by expanding the region around the position of the target.

P2B [9] uses a point-wise network to process points in target and search regions to create a similarity map and find

potential target centers. These regions are then used by a voting algorithm to find the best position candidate.

BAT [14] is a 3D tracking method based on P2B, which uses Box Cloud representations as point features, i.e., a representation which depicts the distances between the points of an object and the center and corners of its 3D bounding box.

3D-SiamRPN [5] uses a Siamese point-wise network to create features for target and search point clouds. It then uses a cross-correlation algorithm to find points of the target in a new frame. An additional region proposal subnetwork is used to regress the final bounding box.

The F-siamese tracker [15] aims to fuse RGB and point cloud information for 3D tracking and applies a 2D Siamese model to generate 2D proposals from an RGB image, which are then used for 3D frustum generation. The proposed frustums are processed with a 3D Siamese model to get the 3D object position.

Point-Track-Transformer (PTT) [10], [16] creates a transformer module for point-based SOT methods and employs it based on a P2B model, leading to an increased performance.

3D Siam-2D [17] uses two Siamese networks, one that creates fast 2D proposals in BEV space, and another one that uses projected 2D proposals to identify which of the proposals belong to the object of interest. The loss of information that occurs in BEV projection affects the performance of the 2D Siamese network. Although voxel pseudo images lie on the BEV space, they do not have this problem, as each pixel of this image incorporates information about the points in a corresponding voxel via a small neural network, and not the projection alone.

Recent works on 3D SOT focus on improving speed as well as tracking performance, but most do not take into consideration the limited computational capabilities of embedded devices, like the NVIDIA Jetson series, which are commonly used in robotics applications. Large delays in processing incoming frames can lead to dropped frames, which can quickly lead to performance degradation of traditional trackers as larger and larger offsets must be predicted as time progresses. In 2D tracking, this concept has been investigated, for example in the real-time experiments of the VOT benchmarks [18], and more recently in [11] for streaming perception tasks in general. In this work, we extend this notion to 3D SOT, and design VPIT to be used efficiently and effectively on embedded devices. Furthermore, to the best of our knowledge, VPIT is the first tracker to use a siamese architecture on point cloud pseudo images directly, while using varying rotations of the target area to find the target’s rotation in subsequent frames. VPIT can be seen as a 3D extension of 2D siamese-based trackers [6], [19], paving the way for other 2D approaches to be successfully extended to the 3D case, while maintaining high tracking speed, even on embedded devices.

III. PROPOSED METHOD

Our proposed method is based on a modified PointPillars architecture for 3D single object tracking, which is originally trained for 3D object detection. In the following subsections,

we first introduce our proposed modifications to the baseline architecture to shift from detection to tracking, and then describe the training and inference processes. Implementation of our method is publicly available in the OpenDR toolkit¹.

A. Model architecture

Point cloud data is irregular and cannot be processed with 2D convolutional neural networks directly. This forces methods to either structure the data using techniques such as voxelization [20]–[23], or to use neural networks that work well on unordered data, such as MLPs with maximum pooling operations or Transformers [5], [9], [10], [24], [25].

Existing datasets for 3D object detection and tracking, such as KITTI [26] and NuScenes [27], consider only a single rotation angle: around the vertical axis. This limitation raises from the nature of scenes in these datasets, as they present data for outdoor object detection and tracking with objects moving on roads. These objects are mostly rotated in Bird’s-eye View (BEV) space, and therefore only this rotation is considered for simplicity.

Since the rotation is limited to the BEV space, we can perform 2D-like Siamese tracking on a structured point cloud representation, such as PointPillars pseudo image [21]. This image is the result of voxelization, where the vertical size of each voxel takes up the whole vertical space, and therefore creating a 2D map in BEV space where each pixel represents a small subspace of a scene and points inside it. Objects in such an image have constant size, as they are not affected by projection size distortions, but their rotation makes the Axis-Aligned Bounding Boxes (AABB) tracking impractical.

Siamese models use an identical transformation $\theta(\cdot)$ to both inputs x and z , which are then combined by some function $g(\cdot)$, i.e. $f(x, z) = g(\theta(x), \theta(z))$. Siamese tracking methods select $\theta(\cdot)$ to be an embedding function and $g(\cdot)$ to be a similarity measure function. If the input x is considered to be a target image that we want to find inside the search image z , the output of such model is a similarity score map, that has high values on the most probable target object locations.

Tracking is performed by first initializing the target region t_0 with the given object location and a corresponding search region $s_0 = \sigma(t_0)$ that should be big enough to accommodate for possible object position offset during the time difference between the input frames. For the frames $F_{\tau-1}$ and F_τ , the target region from previous frame $t_{\tau-1}$ and the corresponding search region $s_{\tau-1}$ are processed by applying the Siamese model to create next target and search regions:

$$\begin{aligned} t_\tau &= t_{\tau-1} + \delta(f(\xi_t(t_{\tau-1}), \xi_s(s_{\tau-1}))), \\ s_\tau &= \sigma(t_\tau), \end{aligned} \quad (1)$$

where the $\delta(\cdot)$ function transforms the similarity map into the target position offset and $\xi_t(\cdot)$ and $\xi_s(\cdot)$ functions transform the target and search regions, respectively, into an image which is processed by the embedding function $\theta(\cdot)$. More details about these functions in Section III-B. This process is repeated for each new frame to update the object location.

SiamFC [6] uses a fully convolutional network as $\theta(\cdot)$ and creates a set of search regions for each target to address the possible change in size due to the projection distortion. We follow the approach of SiamFC and use PointPillars [21] to structure point clouds by generating voxel pseudo image, which serves as an input to the Siamese model, that uses a reduced PointPillars’ Region Proposal Network (RPN) as $\theta(\cdot)$ and a similarity function $g(a, b) = a \otimes b$, where \otimes indicates the correlation operator. In practice, because most DL frameworks perform correlation in convolutional layers, the similarity function can be implemented as $g(a, b) = \text{conv2D}_{\omega=b}(a)$, where ω are the weights of the layer.

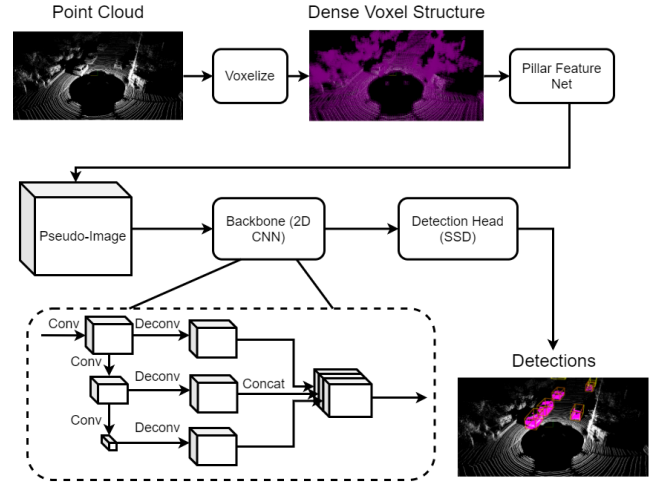


Fig. 1: Structure of PointPillars 3D object detection model. The RPN is a 2D CNN that takes a pseudo image as input.

The Region Proposal Network (RPN) in PointPillars is responsible for processing the input pseudo image using a fully convolutional network with 3 blocks of convolutional layers and 3 transposed convolutions that create same-sized features for final box regression and classification, as can be seen in Fig. 1. For Siamese tracking purposes, we are only interested in feature generation and there is no need for box regression and classification parts of the RPN. Therefore, we select convolutional blocks of the RPN to be used as a Feature Generation Network (FGN) $\theta(\cdot)$. The architecture of the model is shown in Fig. 2. The initial pipeline is similar to PointPillars for Detection, which includes voxelization of the input point cloud and processing it with the Pillar Feature Network to create a voxel pseudo image. The target and search regions of the pseudo image are processed by a Feature Generation Network, creating features that are compared by a cross-correlation module to find a position of the highest similarity, which serves as a new target position.

Each of the target (t) and search (s) regions are represented by a set of 5 values (x, y, w, h, α) , where (x, y) is the position of the region center in pseudo image space in pixels, (w, h) is the size of the region and α is the rotation angle. The ground truth bounding box B_{gt} is described by the 3D position (x, y, z) , size (w, h, d) and rotation α . The corresponding

¹<https://github.com/opendr-eu/opendr>

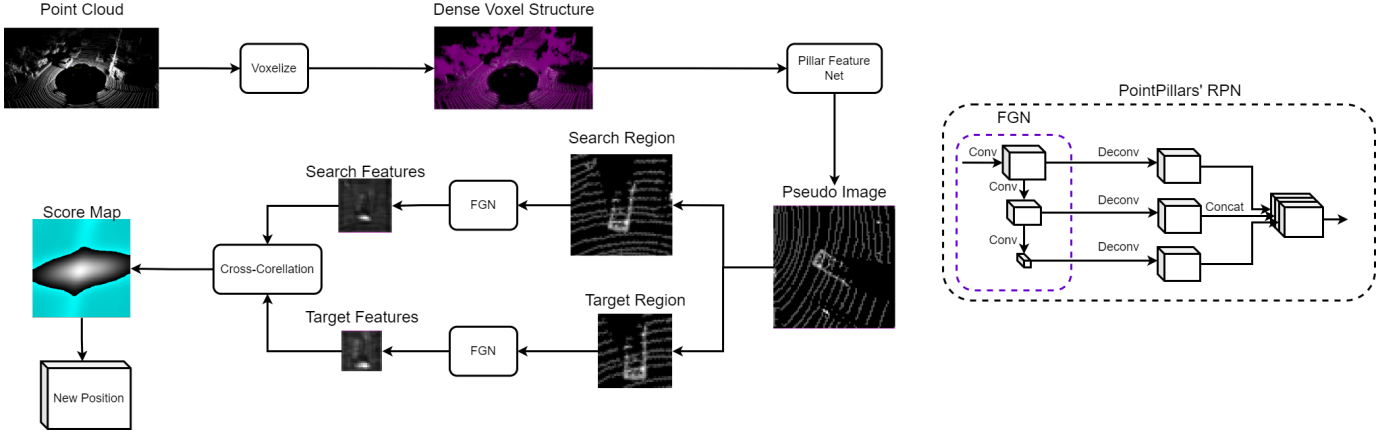


Fig. 2: Structure of the proposed Voxel Pseudo Image Tracking model. The input point cloud is voxelized and processed with the PointPillars' Pillar Feature Network to create a voxel pseudo image, which serves as an input to the Siamese model. The Feature Generation Network (FGN), which is a convolutional subnetwork of the Pointpillars' RPN, processes the target and search regions to create corresponding features that are then compared to find a position of the best similarity.

target and search regions are created as follows:

$$\begin{aligned} t_0 &= \kappa_c((B_{gt}^x, B_{gt}^y, B_{gt}^w, B_{gt}^h, B_{gt}^\alpha)), \\ s_0 &= \sigma(t_0), \end{aligned} \quad (2)$$

where t_0 is the initial target region, s_0 is the initial search region and the $\kappa_c(\cdot)$ is a function that adds context to the target region based on the amount of context parameter c :

$$\begin{aligned} \kappa_c(t) &= \begin{cases} \kappa_{c+}(t), & \text{if } c > 0, \\ \kappa_{c-}(t), & \text{otherwise,} \end{cases} \\ \kappa_{c+}(x, y, w, h, \alpha) &= (x, y, m_n, m_n, \alpha), \\ m_n &= \sqrt{(w+m)(h+m)}, \\ m &= c(w+h), \\ \kappa_{c-}((x, y, w, h, \alpha)) &= (x, y, w(1-c), h(1-c), \alpha), \end{aligned} \quad (3)$$

where $\kappa_{c+}(\cdot)$ adds context to the object by making a square region that includes the original region inside, and $\kappa_{c-}(\cdot)$ adds context by increasing each side of the region independently. The $\sigma(\cdot)$ function creates a search region, the size of which is defined by a hyperparameter σ_s indicating the search region to target region size ratio, i.e.,:

$$\sigma(x, y, w, h, \alpha) = (x, y, \sigma_s w, \sigma_s h, \alpha). \quad (4)$$

The predicted output for the frame τ is computed as:

$$B_\tau = (t_\tau^x, t_\tau^y, B_{gt}^z, t_\tau^w, t_\tau^h, B_{gt}^d, t_\tau^\alpha). \quad (5)$$

B. Training

We start from a pretrained PointPillars model on KITTI Detection dataset. The training can be performed on both KITTI Detection and KITTI Tracking datasets. Training on KITTI Detection dataset is done by considering objects separately and creating target and search region from their bounding boxes. For a set of ground truth boxes $\{B_{\mu_i} | i \in [1, N]\}$ in an input frame μ , where N is a number of ground truth objects in this

frame, we create N training samples by considering target-search pairs $\{(t_{\mu_i}, s_{\mu_i}) | i \in [1, N]\}$ created from these ground truth boxes as follows:

$$\begin{aligned} t_{\mu_i} &= \kappa_c((B_{\mu_i}^x, B_{\mu_i}^y, B_{\mu_i}^w, B_{\mu_i}^h, B_{\mu_i}^\alpha)), \\ s_{\mu_i} &= \sigma_a(\sigma(t_{\mu_i}), t_{\mu_i}), \end{aligned} \quad (6)$$

where $\kappa_c(\cdot)$ and $\sigma(\cdot)$ functions are identical to the ones, described before, and $\sigma_a(\cdot)$ represents an augmentation technique where the center of the search region is shifted from the target center to imitate object movement between frames:

$$\sigma_a(s, t) = (t^x + \epsilon_x, t^y + \epsilon_y, s^w, s^h, s^\alpha), \quad (7)$$

with $\epsilon_x \sim \text{uniform}(-\frac{s^w-t^w}{2}, \frac{s^w-t^w}{2})$ and $\epsilon_y \sim \text{uniform}(-\frac{s^h-t^h}{2}, \frac{s^h-t^h}{2})$. In addition to the proposed augmentation, we use point cloud and ground truth boxes augmentations used in PointPillars, which include point cloud translation, rotation, point and ground truth database sampling.

For training on KITTI tracking dataset, we select the target and search regions from the same track k and object o_k , but the corresponding point clouds and bounding boxes are taken from the different frames, modeling the variance of target object representation in time:

$$\begin{aligned} t_{o_k} &= \kappa_c((B_{f_t}^x, B_{f_t}^y, B_{f_t}^w, B_{f_t}^h, B_{f_t}^\alpha)), \\ \hat{t}_{o_k} &= \kappa_c((B_{f_s}^x, B_{f_s}^y, B_{f_s}^w, B_{f_s}^h, B_{f_s}^\alpha)), \\ s_{o_k} &= \sigma_a(\sigma(\hat{t}_{o_k}), \hat{t}_{o_k}), \end{aligned} \quad (8)$$

where f_t and f_s are a randomly selected frames from the track k that contain the object of interest o_k . We balance the number of occurrences of the same object by selecting a constant number of (f_t, f_s) samples for each object in the dataset.

After creating target and search regions, we apply $\xi_t(\cdot)$ and $\xi_s(\cdot)$ functions by first taking sub-images of those regions and

then, depending on the interpolation size parameter, applying bicubic interpolation to have a fixed size of the image:

$$\begin{aligned} \nu(x) &= \text{subimage}(\Pi(x), x), \\ \xi_\rho(x) &= \begin{cases} \text{bicubic}(\nu(x), \iota_\rho), & \text{if } \iota_\rho > 0, \\ \nu(x), & \text{otherwise,} \end{cases} \end{aligned} \quad (9)$$

where x is a region to be processed, ρ indicates that either target region t , or search region s is selected, ι_ρ is an interpolation size parameter, which indicates the output size of the bicubic interpolation, and $\Pi(x)$ creates an AABP pseudo image from the input point cloud that contains the region x . These images are processed with the Feature Generation Network, which is the convolutional subnetwork of the PointPillars' RPN, as shown in Fig. 2.

The resulting features are compared using the cross-correlation module to create a score map. A Binary Cross-Entropy (BCE) loss is used to compare a predicted score map M_x to the true label M_y as follows:

$$\begin{aligned} BCE(M_x, M_y) &= \frac{1}{N} \sum_1^N l_n, \\ l_n &= -w_n \left(M_{y_n} \log S(M_{x_n}) + (1 - M_{y_n}) \log(1 - S(M_{x_n})) \right), \end{aligned} \quad (10)$$

where $S(x) = 1/(1 + e^{-x})$ and w_n is a scaling weight for each element. We follow SiamFC [6] and select the values of w_n to equalize the total weight of positive and negative pixels on the ground truth score map.

The true label is created by placing positive values on a score map within a small distance of the projected target center, and zeros everywhere else. The value $v(p_x, p_y)$ of a pixel (p_x, p_y) in a label map depends on its distance to the target center $d(p_x, p_y)$ and a hyperparameter r , which describes the radius of positive labels around the center:

$$\begin{aligned} v(x, y) &= \begin{cases} v_{\min} \frac{d(p_x, p_y)}{r} + v_{\max} \left(1 - \frac{d(p_x, p_y)}{r} \right), & \text{if } d(p_x, p_y) \leq r + 1, \\ 0, & \text{otherwise,} \end{cases} \\ d(p_x, p_y) &= \sqrt{(p_x - c_x)^2 + (p_y - c_y)^2}, \end{aligned} \quad (11)$$

where (c_x, c_y) is the target center, $[v_{\min}, v_{\max}]$ is the range of values assigned to the pixels inside the circle of radius r , and the pixels inside the $(r, r + 1]$ range are assigned to values, lower than v_{\min} .

C. Inference

Inference is split into two parts, i.e., initialization and tracking. The 3D bounding box of the object of interest is given by either a detection method, a user, or from a dataset, to create the initial target and its features, that will be used for the future tracking. During tracking, the last target position is used to place a search region, but instead of using only a single search region, we create multiple search regions with identical size and different rotations. This is done to allow to correct for rotation changes in the object. The set of $2K + 1$ search

regions $\{s_{\tau_i} \mid i \in [-K, K]\}$ is created by altering the initial search region s_{τ_0} , i.e., $s_{\tau_i}^{x,y,w,h} = s_{\tau_0}^{x,y,w,h}$ and $s_{\tau_i}^\alpha = s_{\tau_0}^\alpha + i\psi_\alpha$, where ψ_α is a rotation step between consequent search regions.

Target features are compared with all search features, and the one with the highest score is selected for a new rotation:

$$\begin{aligned} s_{\tau_{\max}} &= \underset{s_{\tau_i}}{\operatorname{argmax}} \Lambda_i \max(f(\xi_t(t_\tau), \xi_s(s_{\tau_i}))), \\ t_{\tau+1}^\alpha &= \mu s_{\tau_{\max}}^\alpha + (1 - \mu) t_\tau^\alpha, \end{aligned} \quad (12)$$

where Λ_i is a rotation penalty multiplier, which is 1 for $i = 0$ and a hyperparameter value in $[0, 1]$ range for all other search regions, μ is a rotation interpolation coefficient and f is a Siamese model.

The score map M , obtained from the Siamese model, is upscaled with bicubic interpolation, increasing its size 16 times by default (score upscale parameter u_M). Based on the assumption that an object cannot move far from its previous position in consecutive frames, we use a penalty technique for the scores that are far from the center, by multiplying scores with a weighted penalty map. The penalty map is formed using either Hann window or a 2D Gaussian function. The maximum score position $(x, y)_{\max}$ of the upscaled score map is translated back from the score coordinates to image coordinates as follows:

$$\begin{aligned} (x, y)_{\max} &= \underset{(x, y)}{\operatorname{argmax}} H(f(\xi_t(t_\tau), \xi_s(s_{\tau_{\max}}))), \\ (x, y)_{\max}^{\text{img}} &= (x, y)_{\max} \frac{s_{\tau_{\max}}^{(w, h)}}{H_{\text{size}}}, \\ H_{\text{size}} &= u_M M_{\text{size}}, \\ H(M) &= \eta P(H_{\text{size}}) + (1 - \eta) \text{bicubic}(M, u_M, M_{\text{size}}), \end{aligned} \quad (13)$$

where $(x, y)_{\max}^{\text{img}}$ is a target position offset, which represents a prediction of the target object's movement, H applies score interpolation and a penalty map $P(\text{size})$ to the upscaled output of the Siamese model, M_{size} and H_{size} are the 2D sizes of the original score map and the upscaled score map, respectively, and η is a window influence parameter that controls how much the Hann window or a Gaussian penalty influence the score map.

After the current frame's prediction is ready, the search region is centered on a prediction, assuming that the object's position on the next frame should be close to its position on the previous frame. In order to make it easier to find the position of an object inside a search region, we apply a linear position extrapolation for the search region by centering it not on a previous prediction, but on a possible new prediction position. Given a target region from the last frame $t_{\tau-1}$ and the predicted target region t_τ , the corresponding search region has its position defined $s_\tau^{x,y} = 2t_\tau^{x,y} - t_{\tau-1}^{x,y}$. This approach increases the chances of the target to be in the center of the search region or having a small deviation from it.

When the linear extrapolation is used, the penalty map $P(\text{size})$ (Eq. 13) is created using a 2D Gaussian with a covariance matrix Σ that represents the angle of the extrapolation vector to penalize more positions that are not on the way of the predicted object's movement. This is done by creating a

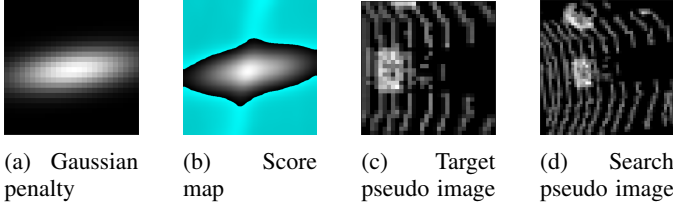


Fig. 3: An example of a directional Gaussian penalty used with linear extrapolation, a corresponding score map and target and search pseudo images. Cyan color on the score map represents negative values.

Gaussian with independent variables and variances σ_+ for the desired direction and σ_- for the opposite direction:

$$\mu = 0 \quad \text{and} \quad \Sigma_0 = \begin{bmatrix} \sigma_- & 0 \\ 0 & \sigma_+ \end{bmatrix}. \quad (14)$$

Bigger σ_+ allows a further offset alongside the extrapolation vector, while bigger σ_- allows a higher deviation from it. The resulting Gaussian $\mathcal{N}(\mu, \Sigma_0)$ is rotated by $\phi = \arctan(e)$, where e is the extrapolation vector, as follows:

$$R = \begin{bmatrix} \cos(\phi) & -\sin(\phi) \\ \sin(\phi) & \cos(\phi) \end{bmatrix} \quad \text{and} \quad \Sigma = R\Sigma_0^{-1}R^T. \quad (15)$$

The creation of such a map for a high-dimensional upscaled score map is a computationally expensive task, and therefore, to optimize it, the penalty maps are hashed by their size and rotation to reuse in future frames. There is no need in keeping high precision of rotation value, as the penalty map will be almost identical for close ϕ values and will result in the same basis for predictions. Keeping this in mind, we define a rotation hash function $H_r(\phi) = \left\lfloor \frac{n\phi}{2\pi} \right\rfloor$. This hash function divides the full circle on n equal regions, and the penalty map is taken for the closest ϕ -sector. Fig. 3 shows an example of a Gaussian penalty created using this approach, a corresponding score map and target and search pseudo images.

Target features are created at the first frame and then used to find the object during the whole tracking sequence. However, due to a high variance of object representation on different distances to Lidar, initial features may be too far from the current representation of the object, as can be seen from Fig. 4. This problem may be resolved by using target features from the latest frame, but such approach leads to an error accumulation and drifts the target region to a background object. In order to balance between the aforementioned approaches, we introduce a target feature merge scale m_{tf} . Using the $m_{tf} = 0$, only the initial target features will be used through the tracking task, while using the $m_{tf} = 1$ results in the latest frame’s target features overwriting the previous ones. Fig. 5 shows the effect of a high merge scale value $m_{tf} = 0.5$. The target region is slowly drifting to the right starting from frame 10 and the object is completely lost at frame 30. We use small values of m_{tf} in range $[0, 0.01]$ in ablation study. This allows to keep the target features stable and not drift out from the object, while still having the possibility to update features if the distance to the object changes.

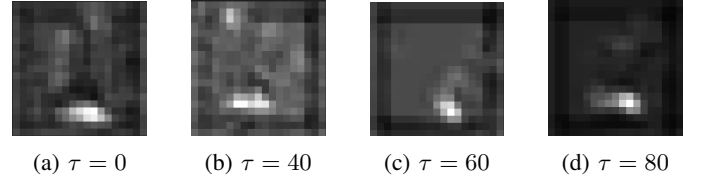


Fig. 4: Target features of the same object at different frames.

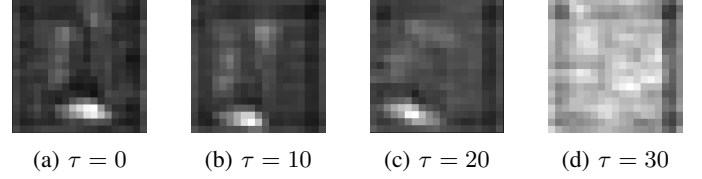


Fig. 5: Merged target features of the same object at different frames with 0.5 merge scale. Starting from frame 10, the object representation drifts to the right and completely loses the target at frame 30.

By default, the model’s position offset predictions are applied directly, but we can improve prediction stability by introducing the offset interpolation parameter ω . Given the previous frame’s target position $\zeta_{\tau-1}$ and a prediction for the current frame $\hat{\zeta}_\tau$, the interpolated position ζ_τ is defined as follows:

$$\zeta_\tau = \omega\zeta_{\tau-1} + (1 - \omega)\hat{\zeta}_\tau. \quad (16)$$

Current 3D detection and tracking datasets provide annotations for a rotation around the vertical axis only, which is sufficient for current robotic and autonomous driving tasks, but it may be too coarse for future tasks. For datasets with rotations around all axes and not only the vertical one, an additional regression branch can be added that, applied to a target region, will predict other rotation angles. A similar process can be applied to non-rigid objects in order to continuously update their dimensions.

TABLE I: Results of 3D Car tracking on KITTI dataset. Modality represents the type of data the tracking is performed on (PC for point cloud, BEV for Birds-Eye-View and VPI for voxel pseudo image). FPS values are reported on a 1080Ti GPU by a corresponding paper. FPS values with a star notation are obtained by running the methods’ official implementations on a 1080ti GPU considering the full runtime of the network.

Method	Modality	Success	Precision	FPS
3DSRPN PCW [5]	PC	56.32	73.40	16.7
3DSRPN PW [5]	PC	57.25	75.03	20.8
SCD3D-KF [13]	PC	40.09	56.17	2.2
SCD3D-EX [13]	PC	76.94	81.38	1.8
3D Siam-2D [17]	PC+BEV	36.3	51.0	-
BAT [14]	PC	65.38	78.88	23.96*
PTT-Net [10]	PC	67.8	81.8	39.51*
P2B [9]	PC	56.2	72.8	30.18*
VPIT (Ours)	VPI	50.49	64.53	50.45

TABLE II: Evaluation of the fastest methods for 3D Car tracking on KITTI dataset. The evaluation is performed with official implementations on high-end and embedded GPU platforms with different combinations of GPU/CPU. 32C CPU and 104C CPU correspond to 32-core and 104-core CPUs, respectively.

Method	Modality	Success	Precision	FPS				
				1080Ti 32C CPU	2080 32C CPU	2080Ti 104C CPU	TX2	Xavier
P2B [9]	PC	56.2	72.8	30.18	26.34	38.93	6.20	10.37
PTT-Net [10]	PC	67.8	81.8	39.51	33.34	50.25	8.04	13.49
VPIT (Ours)	VPI	50.49	64.53	50.45	52.52	72.53	14.61	20.55

IV. EXPERIMENTS

We use KITTI [26] Tracking training dataset split to train and test our model, with tracks 0-18 for training and validation and tracks 19-20 for testing (as is common practice [5], [9], [10], [13], [17]). We use Precision and Success metrics as defined in One Pass Evaluation [28]. Precision is computed based on the difference between ground-truth and predicted object centers in 3D. Success is computed based on the 3D Intersection over Union (IoU) between predicted and ground truth 3D bounding boxes.

We use 1 feature block from the original PointPillars model with 4 layers in a block. The model is trained for 64,000 steps with BCE loss, $1 * 10^{-5}$ learning rate and 2 positive label radius. During inference, rotations count of 3, rotation step of 0.15 and rotation penalty of 0.98 are used, together with 0.85 penalty map multiplier, score upscale of 8, target/search size of (0,0) (original sizes are used), context amount of 0.27, rotation interpolation of 1, offset interpolation of 0.3, target feature merge scale of 0.005 and linear search position extrapolation.

A. Comparison with state-of-the-art

Evaluation results on 1080Ti GPU are given in Table I. Even though we are interested in embedded devices, we first measure FPS on a 1080Ti, since this is the most commonly used GPU amongst the compared methods, as a relative speed measure between them. VPIT is the fastest method and achieves competitive Precision and Success. We evaluate official implementations of the fastest methods (P2B, PTT, VPIT) on different high-end and embedded GPU platforms to showcase how the architecture of the device influences the models' FPS.

When computing FPS, we include all the time the model spends to process the input and create a final result. This excludes time spend to obtain data and to compute Success and Precision values, but includes pre- and post-processing steps.

As can be seen from Table II, in terms of speed, VPIT outperforms P2B by 67% on 1080Ti GPU, 99% on 2080 GPU and 86% on 2080Ti GPU with 104-core CPU. For embedded devices, the difference is bigger: VPIT outperforms P2B by 135% on TX2 and by 98% on Xavier. This indicated that the approach of VPIT is more suited to the robotic systems, where embedded devices are the most common, and it is harder to meet real-time requirements.

B. Real-time evaluation

Application of 3D tracking methods is usually done for robotic systems that do not use high-end GPUs due to their high power consumption, but instead apply the computations on embedded devices, such as TX2 or Xavier. Following [11] we implement a predictive real-time benchmark. Given a time step τ , the set of inputs S_{in} that is visible to the model is limited by those inputs that appeared before τ , i.e., $S_{in} = (x_i, \tau_i | i \leq \tau)$, where (x_i, τ_i) is a pair of an input frame and a corresponding time step. The processing time of the model is higher than zero, which means that the resulting prediction p_i at time $\hat{\tau}_i$ cannot be compared to the label y_i from the same frame, and therefore for each label y_i from the dataset, it will be compared to the latest prediction $p_{l_{pr}(i)}$. The predictive real-time error E_{pr} , based on a regular error E , is computed for each ground truth label y_i as follows:

$$\begin{aligned} E_{pr}(y_i) &= E(y_i, p_{l_{pr}(i)}), \\ l_{pr}(i) &= \underset{j}{\operatorname{argmax}} \hat{\tau}_j \leq \tau_i. \end{aligned} \quad (17)$$

As shown in [11], the existing model can be improved for a predictive real-time evaluation by predicting the position of the object at a frame i and then predicting its movement during the time period between the frames i and $i+1$ using a Kalman Filter [29] or any other similar method. Such optimization can be applied to any of the methods that we compare, and therefore, to eliminate the factor of “predictive errors” where the model’s error in prediction for the current frame is more leaned towards the prediction for the next frame, we introduce a non-prediction real-time benchmark. This benchmark effectively shifts all labels one frame forward, allowing the methods that are faster than the data FPS to be evaluated in the same way, as in a regular evaluation protocol. The only difference between the non-predictive and predictive benchmarks is in the way the latest prediction is defined:

$$l_{npr}(i) = \underset{j}{\operatorname{argmax}} \hat{\tau}_j \leq \tau_{i+1}. \quad (18)$$

We evaluate the fastest 3D SOT methods (P2B, PTT, VPIT) on embedded devices with both non-predictive (Table III) and predictive (Table IV) benchmarks. We select Data FPS to be either 10 or 20, representing the most popular 10 and 20 Hz Lidars. The 10Hz Lidar is the easier case, as for the method to be real-time, it needs to sustain FPS, higher than 10, compared to 20 for the 20 Hz Lidar. During the evaluation, we compute

TABLE III: Evaluation of the fastest methods for 3D Car tracking on KITTI dataset in real-time settings without the predictive requirement. The evaluation is performed with official implementations on embedded GPU platforms for 10 and 20 Hz Lidars (Data FPS). Frame drop represents the percentage of frames that could not be processed due to the model’s latency. Regular represents evaluation without real-time requirements.

Method	Data FPS	Success (non-predictive)			Precision (non-predictive)			FPS		Frame drop	
		Regular	TX2	Xavier	Regular	TX2	Xavier	TX2	Xavier	TX2	Xavier
P2B [9]	10	56.20	21.90	36.50	72.80	21.70	42.40	6.17	10.07	37.41%	7.00%
PTT-Net [10]	10	67.80	29.50	63.60	81.80	30.00	75.10	6.90	12.38	28.21%	0.81%
VPIT (Ours)	10	50.49	50.31	50.49	64.53	64.08	64.53	14.31	20.55	0.68%	0.00%
P2B [9]	20	56.20	10.90	16.70	72.80	7.90	15.0	5.54	9.61	70.57%	51.56%
PTT-Net [10]	20	67.80	17.90	26.50	81.80	15.70	26.60	6.61	11.88	64.14%	38.95%
VPIT (Ours)	20	50.49	38.96	47.70	64.53	45.50	59.87	14.37	20.06	30.17%	2.38%

TABLE IV: Evaluation of the fastest methods for 3D Car tracking on KITTI dataset in real-time settings with the predictive requirement. The evaluation is performed with official implementations on embedded GPU platforms for 10 and 20 Hz Lidars (Data FPS). Frame drop represents the percentage of frames that could not be processed due to the model’s latency. Regular represents evaluation without real-time requirements

Method	Data FPS	Success (predictive)			Precision (predictive)			FPS		Frame drop	
		Regular	TX2	Xavier	Regular	TX2	Xavier	TX2	Xavier	TX2	Xavier
P2B [9]	10	56.20	19.10	30.30	72.80	17.80	33.70	6.17	10.07	36.31%	6.79%
PTT-Net [10]	10	67.80	24.90	50.70	81.80	23.40	59.00	7.07	12.26	26.15%	0.90%
VPIT (Ours)	10	50.49	45.82	46.68	64.53	57.76	59.28	14.61	20.55	0.57%	0.00%
P2B [9]	20	56.20	9.10	13.50	72.80	6.00	10.90	5.54	9.47	69.57%	50.31%
PTT-Net [10]	20	67.80	15.40	23.20	81.80	13.10	21.50	6.67	12.06	62.49%	37.35%
VPIT (Ours)	20	50.49	34.00	41.39	64.53	36.61	49.36	14.40	20.77	29.41%	1.56%

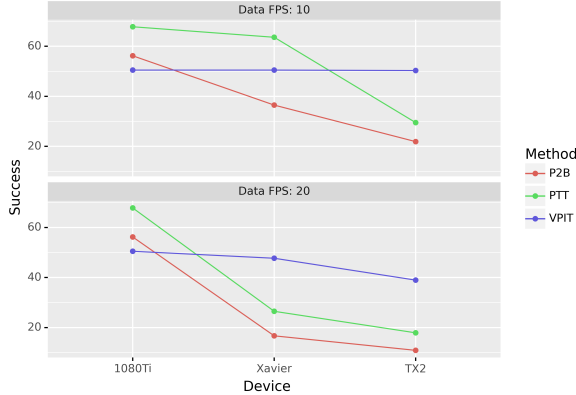


Fig. 6: Evaluation of the fastest models with real-time requirements on embedded devices and a desktop GPU. Data FPS represents 10 and 20 Hz Lidars. Devices are sorted in descending order by their computational power.

how many frames could not be processed due to the model’s latency and represent it as a Frame drop percentage.

Only VPIT on Xavier (more powerful embedded device) for a 10Hz Lidar could not suffer from any frame drop, resulting in the regular Success and Precision values for a non-predictive benchmark and suffering 3.81 Success and 5.25 Precision for a predictive benchmark. The highest Frame drop of 60 – 70% is seen for P2B and PTT on TX2 for a 20Hz Lidar. In this case, Success values of P2B and PTT are 6 and 4 times lower than during the regular evaluation, respectively, which indicates that these methods cannot work under the aforementioned conditions. For every evaluation case, except the Xavier with

a 10Hz Lidar, VPIT outperforms P2B and PTT in Success, Precision, FPS and Frame drop, but PTT still maintains the best Success and Precision on Xavier with a 10Hz Lidar. As can be seen from Fig. 6, Success drop of VPIT is the smallest, while P2B and PTT lose most of their tracking accuracy on TX2 for any Lidar and on Xavier for a 20Hz Lidar.

Evaluation of the other methods, presented in Table I, is not needed, as their FPS is 2 or more times slower than the FPS of P2B and PTT, which will result in a complete loss of Success and Precision on any of the real-time benchmarks that were discussed.

C. Ablation study

We performed experiments to determine the influence of different hyperparameters on the Success and Precision metrics. We used KITTI Tracking tracks 10 – 11 for validation and 0 – 9, 12 – 18 for training. The influence of selected hyperparameters on Success and Precision metrics is similar, and therefore we present only the effect on Success metric on validation subset in Fig. 7.

Decreasing the number of feature blocks from the Feature Generation Network, leads to better Success values. This can be due to an increasing receptive field with each new block that leads to over smoothing of the resulting feature maps and makes it harder to define a precise position of an object of interest.

Next, we follow SiamFC [6] and use target and search upscaling with $\iota_t = (127, 127)$ and $\iota_s = (255, 255)$. This results in constant-sized target and search pseudo-images, corresponding feature and score maps, which allows implementing mini-batch training and reduce the training time.

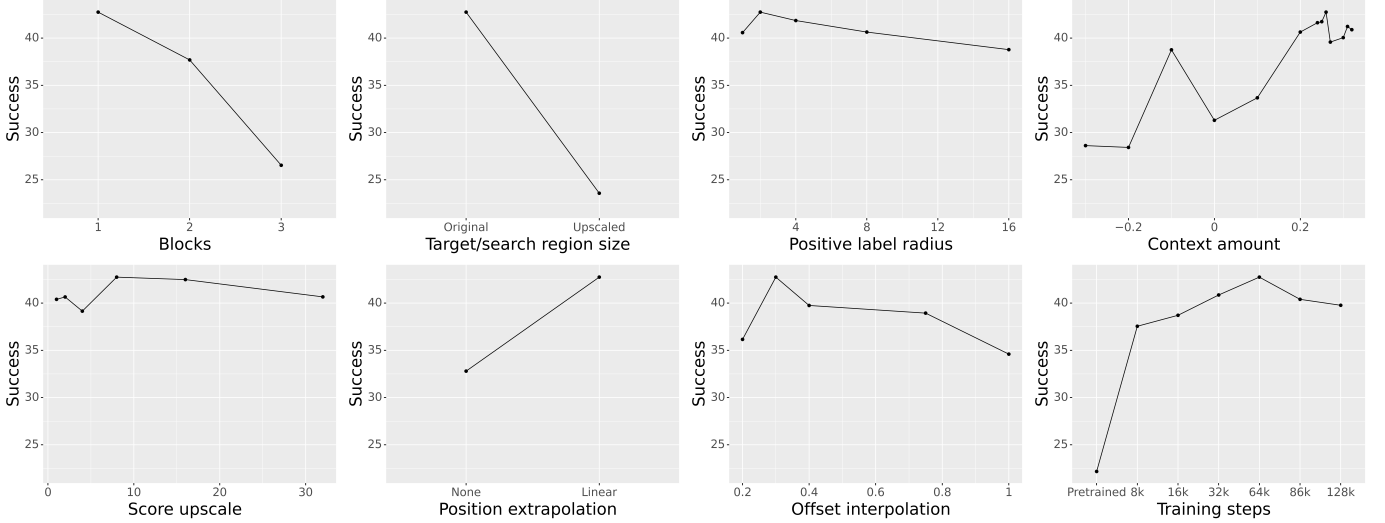


Fig. 7: Influence of different hyperparameter values on Success metric on validation KITTI Tracking subset.

However, such approach does not work well for voxel pseudo images, achieving 81% less Success than when using original sizes ($\iota_t = (0, 0)$ and $\iota_s = (0, 0)$).

Furthermore, following SiamFC [6], positive values of the context amount parameter c result in square target and search regions. In contrast to it, we also use negative c values to add independent context to each dimension of the region, keeping its aspect ratio. Positive context leads to better Success with the maximum at $c = 0.26$, which is 10% higher than the result for $c = -0.1$.

Regarding the positive label radius, $r = 2$ results in the best training procedure, but this hyperparameter has a low influence on the final Success value, as well as the target feature merge scale m_{tf} , window influence η , score upscale u_M , search region scale σ_s , rotation step ψ_α and rotation penalty Λ .

Next, linear position extrapolation leads to a 30% increase in Success compared to a conventional search region placement and no directional penalty. With offset interpolation $\omega = 0.3$, the Success value increases by 24%, compared to the direct application of the model’s prediction ($\omega = 1$).

Finally, a pretrained PointPillars backbone creates features that are capable of differentiating between target class and other object types, but those features cannot be used effectively to differentiate between different objects from the same class. This serves as a good starting point for the SOT task, and then training for 64000 steps results in the best model for selected hyperparameters.

V. CONCLUSIONS

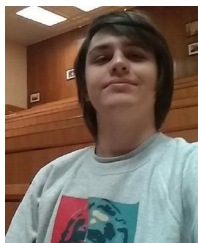
In this work, we proposed a novel method for 3D SOT called VPIT. We focus on stepping out of the point-based approaches for this problem and studying methods to use structured data for 3D SOT. We formulate a lightweight method that uses PointPillars’ pseudo images as a search space and apply a Siamese 2D-like approach on these pseudo images to find both position and rotation of the object of interest.

Experiments show that VPIT is the fastest method, and it achieves competitive Precision and Success values. Moreover, we implement a real-time evaluation protocol for 3D single object tracking and use it for evaluation of the fastest methods on embedded devices, that are the most popular choice for robotic systems. Results showcase that other methods are less suited for such devices and lose most of their ability to track objects due to a high latency of predictions. The proposed method allows for an easy adaptation of 2D tracking ideas to a 3D SOT task while keeping the model lightweight.

REFERENCES

- [1] “Kitti 3d object detection leaderboard,” 2022, [Accessed 26-January-2022]. [Online]. Available: http://www.cvlibs.net/datasets/kitti/eval_object.php?obj_benchmark=3d
- [2] D. S. Bolme, J. R. Beveridge, B. A. Draper, and Y. M. Lui, “Visual object tracking using adaptive correlation filters,” in *2010 IEEE Computer Society Conference on Computer Vision and Pattern Recognition*, 2010, pp. 2544–2550.
- [3] J. F. Henriques, R. Caseiro, P. Martins, and J. Batista, “High-speed tracking with kernelized correlation filters,” *IEEE Transactions on Pattern Analysis and Machine Intelligence*, vol. 37, no. 3, p. 583–596, 2015.
- [4] D. Held, S. Thrun, and S. Savarese, “Learning to track at 100 fps with deep regression networks,” *1604.01802*, 2016.
- [5] Z. Fang, S. Zhou, Y. Cui, and S. Scherer, “3d-siamrpn: An end-to-end learning method for real-time 3d single object tracking using raw point cloud,” *IEEE Sensors Journal*, vol. 21, no. 4, p. 4995–5011, 2021.
- [6] L. Bertinetto, J. Valmadre, J. F. Henriques, A. Vedaldi, and P. H. Torr, “Fully-convolutional siamese networks for object tracking,” *arXiv:1606.09549*, 2016.
- [7] B. Li, J. Yan, W. Wu, Z. Zhu, and X. Hu, “High performance visual tracking with siamese region proposal network,” in *Proceedings of the IEEE conference on computer vision and pattern recognition*, 2018, pp. 8971–8980.
- [8] B. Li, W. Wu, Q. Wang, F. Zhang, J. Xing, and J. Yan, “Siamrpn++: Evolution of siamese visual tracking with very deep networks,” *arXiv:1812.11703*, 2018.
- [9] H. Qi, C. Feng, Z. Cao, F. Zhao, and Y. Xiao, “P2b: Point-to-box network for 3d object tracking in point clouds,” *arXiv:2005.13888*, 2020.
- [10] J. Shan, S. Zhou, Z. Fang, and Y. Cui, “Ptt: Point-track-transformer module for 3d single object tracking in point clouds,” *arXiv:2108.06455*, 2021.
- [11] M. Li, Y.-X. Wang, and D. Ramanan, “Towards streaming perception,” in *European Conference on Computer Vision*. Springer, 2020, pp. 473–488.

- [12] Y. Li, L. Ma, Z. Zhong, F. Liu, M. A. Chapman, D. Cao, and J. Li, "Deep learning for lidar point clouds in autonomous driving: A review," *IEEE Transactions on Neural Networks and Learning Systems*, vol. 32, no. 8, pp. 3412–3432, 2021.
- [13] S. Giancola, J. Zarzar, and B. Ghanem, "Leveraging shape completion for 3d siamese tracking," 2019.
- [14] C. Zheng, X. Yan, J. Gao, W. Zhao, W. Zhang, Z. Li, and S. Cui, "Box-aware feature enhancement for single object tracking on point clouds," in *Proceedings of the IEEE/CVF International Conference on Computer Vision*, 2021, pp. 13 199–13 208.
- [15] H. Zou, J. Cui, X. Kong, C. Zhang, Y. Liu, F. Wen, and W. Li, "F-siamese tracker: A frustum-based double siamese network for 3d single object tracking," in *2020 IEEE/RSJ International Conference on Intelligent Robots and Systems (IROS)*. IEEE, 2020, pp. 8133–8139.
- [16] S. Jiayao, S. Zhou, Y. Cui, and Z. Fang, "Real-time 3d single object tracking with transformer," *IEEE Transactions on Multimedia*, 2022.
- [17] J. Zarzar, S. Giancola, and B. Ghanem, "Efficient bird eye view proposals for 3d siamese tracking," *arXiv:1903.10168*, 2020.
- [18] M. Kristan, J. Matas, A. Leonardis, M. Felsberg, R. Pflugfelder, J.-K. Kämäräinen, H. J. Chang, M. Danelljan, L. Cehovin, A. Lukežič *et al.*, "The ninth visual object tracking vot2021 challenge results," in *Proceedings of the IEEE/CVF International Conference on Computer Vision*, 2021, pp. 2711–2738.
- [19] P. Nousi, A. Tefas, and I. Pitas, "Dense convolutional feature histograms for robust visual object tracking," *Image and Vision Computing*, vol. 99, p. 103933, 2020.
- [20] Y. Zhou and O. Tuzel, "VoxelNet: End-to-End Learning for Point Cloud Based 3D Object Detection," in *IEEE Conference on Computer Vision and Pattern Recognition*, 2018.
- [21] A. H. Lang, S. Vora, H. Caesar, L. Zhou, J. Yang, and O. Beijbom, "PointPillars: Fast Encoders for Object Detection from Point Clouds," in *IEEE Conference on Computer Vision and Pattern Recognition*, 2019.
- [22] Z. Liu, X. Zhao, T. Huang, R. Hu, Y. Zhou, and X. Bai, "TANet: Robust 3D Object Detection from Point Clouds with Triple Attention," in *AAAI Conference on Artificial Intelligence*, 2020.
- [23] Q. Chen, L. Sun, Z. Wang, K. Jia, and A. L. Yuille, "Object as Hotspots: An Anchor-Free 3D Object Detection Approach via Firing of Hotspots," in *European Conference on Computer Vision*, 2020.
- [24] C. R. Qi, H. Su, K. Mo, and L. J. Guibas, "Pointnet: Deep learning on point sets for 3d classification and segmentation," *arXiv:1612.00593*, 2017.
- [25] C. R. Qi, L. Yi, H. Su, and L. J. Guibas, "Pointnet++: Deep hierarchical feature learning on point sets in a metric space," *arXiv:1706.02413*, 2017.
- [26] A. Geiger, P. Lenz, and R. Urtasun, "Are we ready for autonomous driving? The KITTI vision benchmark suite," in *IEEE Conference on Computer Vision and Pattern Recognition*, 2012.
- [27] H. Caesar, V. Bankiti, A. H. Lang, S. Vora, V. E. Liong, Q. Xu, A. Krishnan, Y. Pan, G. Baldan, and O. Beijbom, "nuScenes: A Multimodal Dataset for Autonomous Driving," in *IEEE/CVF Conference on Computer Vision and Pattern Recognition*, 2020.
- [28] M. Kristan, J. Matas, A. Leonardis, T. Vojir, R. Pflugfelder, G. Fernandez, G. Nebehay, F. Porikli, and L. Cehovin, "A novel performance evaluation methodology for single-target trackers," *IEEE Transactions on Pattern Analysis and Machine Intelligence*, vol. 38, no. 11, p. 2137–2155, 2016.
- [29] R. E. Kalman, "A New Approach to Linear Filtering and Prediction Problems," *Journal of Basic Engineering*, vol. 82, no. 1, pp. 35–45, 1960.



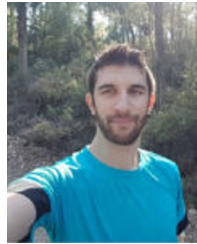
Illia Oleksiienko Received the B.Sc. degree in Informatics from National Pedagogical Dragomanov University, Ukraine in 2018 and M.Sc. degree in Software Engineering from National Technical University of Ukraine "Igor Sikorsky Kyiv Polytechnic Institute", Ukraine in 2019. He is currently pursuing the Ph.D. degree in Electrical and Computer Engineering with the Machine Learning and Computational Intelligence research group, Department of Electrical and Computer Engineering, Aarhus University, Denmark.

His research interests include 3D object detection and tracking, deep learning for embedded devices, AutoML methods and point cloud processing.



Paraskevi Nousi Obtained her B.Sc. and Ph.D. degree in Informatics from the Aristotle University of Thessaloniki in 2014 and 2021 respectively. She is currently a post-doctoral researcher in the Artificial Intelligence and Information Analysis Laboratory in the Department of Informatics at the Aristotle University of Thessaloniki.

Her research interests include deep learning for computer vision, robotics, financial forecasting and gravitational waves analysis.



Nikolaos Passalis (Graduate Student Member, IEEE) Received the B.Sc. degree in informatics, the M.Sc. degree in information systems, and the Ph.D. degree in informatics from the Aristotle University of Thessaloniki, Thessaloniki, Greece, in 2013, 2015, and 2018, respectively.

Since 2019, he has been a post-doctoral researcher with the Aristotle University of Thessaloniki, while from 2018 to 2019 he also conducted post-doctoral research at the Faculty of Information Sciences, Tampere University, Finland. He has (co)authored more than 30 journal articles and 45 conference papers. His research interests include deep learning, information retrieval, time-series analysis and computational intelligence.



Anastasios Tefas (Member, IEEE) received the B.Sc. in Informatics in 1997 and the Ph.D. degree in Informatics in 2002, both from the Aristotle University of Thessaloniki, Greece and since January 2022 he has been a Professor at the Department of Informatics of the same university.

From 2017 until 2021 he was an Associate Professor and from 2008 to 2017 he was a Lecturer at the Aristotle University of Thessaloniki, as well. From 2006 to 2008, he was an Assistant Professor at the Department of Information Management, Technological Institute of Kavala. From 2003 to 2004, he was a temporary lecturer in the Department of Informatics, University of Thessaloniki. Dr. Tefas participated in 20 research projects financed by national and European funds. He is the Coordinator of the H2020 project OpenDR, "Open Deep Learning Toolkit for Robotics". He is Area Editor in Signal Processing: Image Communications journal. He has co-authored 135 journal papers, 247 papers in international conferences and contributed 8 chapters to edited books in his area of expertise. Over 6500 citations have been recorded to his publications and his H-index is 40 according to Google scholar. His current research interests include computational intelligence, deep learning, pattern recognition, statistical machine learning, digital signal and image analysis and retrieval and computer vision.



Alexandros Iosifidis (SM'16) is a Professor at Aarhus University, Denmark. He leads the Machine Intelligence research area at the University's Centre for Digitalisation, Big Data, and Data Analytics. He has contributed to more than 30 research and development projects financed by EU, Finnish, and Danish funding agencies and companies. He has (co-)authored 96 articles in international journals and 120 papers in international conferences, symposia and workshops. He is a member of the IEEE Technical Committee on Machine Learning for Signal

Processing, and the EURASIP Visual Information Processing Technical Area Committee. He is the Associate Editor-in-Chief of Neurocomputing journal covering the research area of neural networks, and an Associate Editor of IEEE TRANSACTIONS ON NEURAL NETWORKS AND LEARNING SYSTEMS.